

# *Chandra* ACIS and *Newton* EPIC Observations of the X-ray Luminous SN1978K in NGC 1313

Eric M. Schlegel, Albert Kong, Philip Kaaret, Rosanne DiStefano, Steve Murray

*High Energy Astrophysics Division, Smithsonian Astrophysical Observatory, Cambridge, MA 02138*

## ABSTRACT

We describe an observation of the X-ray luminous SN1978K in NGC 1313 using the ACIS detector on *Chandra* and an archival *Newton* EPIC observation. The models that provided good fits to the *ASCA* SIS and GIS and the *ROSAT* PSPC spectra no longer do so for the ACIS and EPIC spectra. The best-fit model to the ACIS and EPIC spectra are dual hot plasma models (vmekal); one component is soft ( $T = 0.61_{-0.05}^{+0.04}$  keV, 90% errors) and the other is harder ( $T = 3.16_{-0.40}^{+0.44}$  keV). For the varying abundances permitted within the model, only the Si abundance of the soft component differs from solar, with a value  $n_{\text{SN78K}}^{\text{Si}} / n_{\text{solar}}^{\text{Si}} = 3.20_{-1.90}^{+1.80}$  (90% errors). From a ratio of the low- and high-T model fits to the *Chandra* and *XMM-Newton* spectra, we infer an exponent  $n$  of the ejecta density distribution,  $\rho_{\text{ejecta}} \propto r^{-n}$ , of  $\sim 5.2$  adopting a circumstellar matter distribution exponent of  $s = 2$  ( $\rho_{\text{cs}} \propto r^{-s}$ ). The 0.5-2 keV light curve shows essentially no decline; the 2-10 keV light curve, constructed only of the *ASCA*, *XMM-Newton*, and *Chandra* observations, shows a drop of 1.5 from the *ASCA* epoch. The hard band decline, together with the apparently enhanced Si emission, signal the start of the X-ray decline of SN1978K.

*Subject headings:* supernovae: individual (SN1978K)

## 1. Introduction

X-ray emission may emerge at two stages in the evolution of a supernova: near the time of the shock breakout and via circumstellar interaction at a later date. Three different processes generate X-rays: from the prompt thermal burst; via Compton-scattered  $\gamma$ -rays from the synthesized matter's radioactive decay (from which X-rays are emitted while the debris is optically thick to  $\gamma$ -rays); and from the interaction of the shock with circumstellar material in the vicinity of the progenitor. Only SN1987A has been seen to emit X-rays definitely attributed to Compton-scattered  $\gamma$ -rays (Dotani et al. 1987, *Nature*, 330, 230).

Two mechanisms exist for the circumstellar production of X-rays: X-rays from the outgoing shock or from the reverse shock (Fransson et al. 1996). Below 10 keV, the reverse shock should be the dominant emitter because the density behind the shock is higher, by a factor of  $\sim 4$ , than the

swept-up circumstellar density behind the forward shock. If a cool shell forms because the reverse shock is radiative, that shell absorbs X-rays below 10 keV and the observed 1-10 keV emission must be from the forward shock as discussed for SN1993J (Fransson et al. 1996).

Other than SN1987A, few supernovae have been followed in the X-ray band. The total current pool consists of <20 objects; of those, only four supernovae have data sets consisting of more than four observations (SN1978K, SN1993J, SN1998S, SN1999em; Schlegel 1995; Immler & Lewin 2002). SN1978K is one of a small number of extremely luminous, X-ray emitting supernovae (Schlegel 1995; Immler & Lewin 2002). As X-ray observations are difficult to obtain, each bright supernova contributes valuable knowledge to our understanding of the X-ray emission from supernovae.

The X-ray emission of SN1978K was first uncovered in an observation obtained with the *ROSAT* PSPC in 1992 (Ryder et al. 1993) (hereafter, R93). It had been detected optically during a spectrophotometric survey of H II regions two years earlier and reported as a nova (Dopita & Ryder 1990) at that time. It had also been detected as a powerful radio source in 1982 but never followed up (R93). As part of the investigation spurred by the X-ray detection, examination of archival optical plates uncovered a light curve that while crude was sufficient to assign an explosion date near 1 June 1978 (R93).

To further study SN1978K, observations were obtained during the mid- and late-1990s with *ASCA*, *Hubble Space Telescope*, *ROSAT* (High Resolution Imager), *Australia Telescope Compact Array* (ATCA), and the *Anglo-Australian Observatory* (AAO) covering the X-ray, ultraviolet, optical, and radio bands (Schlegel et al. 1999) (hereafter, S99). An early *ASCA* spectrum and *ROSAT* light curve were reported in Petre et al. (1994) and Schlegel, Petre, & Colbert (1996), respectively. The *ATCA* radio light curve showed behavior typical of a circumstellar interaction, with a rapid turn-on followed by a slow decline at all radio wavelengths (e.g., Weiler et al. 1996; S99). Optically, the *AAO* spectra of SN1978K showed strong emission lines of the Balmer series as well as He I, [O III], [Ne III], and [Fe II] (R93). In the ultraviolet, the Mg II doublet and [Ne IV] lines were detected using the *HST* Faint Object Spectrograph (S99). The X-ray light curve was consistent with no decline throughout the decade (S99). The *ASCA* spectra were best-fit with absorbed, single-component continuum models; no evidence for line emission existed in the data (Petre et al. 1994, S99).

SN1978K is important because it is among the first known X-ray emitting supernovae with luminosities above  $10^{39}$  erg s<sup>-1</sup>. It is also a nearby object and may be studied in greater detail than more distant supernovae.

In this paper, we present the *Chandra* ACIS spectrum of SN1978K and contrast it with the recent *XMM-Newton* and earlier *ASCA* spectra. Throughout we adopt a distance to NGC 1313 of  $4.13 \pm 0.11$  Mpc as determined by Méndez et al. (2002).

## 2. Data

*Chandra* observed NGC 1313 and its X-ray emitting sources on 2002 October 13 for 20592 sec with the ACIS detector (Garmire et al. 2003). The aimpoint of the detector fell on the back-illuminated S3 CCD. We extracted a light curve of the background, masking out all bright sources detectable by eye, to search for any signatures of flaring events known to affect back-illuminated CCDs (Chandra Proposers’ Guide 2002). No strong flares were detected but a few high points were eliminated, reducing the good exposure time to 19902 sec.

We extracted the events at the location of SN1978K, about  $5'.88$  off-axis, in an aperture of radius  $12''$  which encloses  $>98\%$  of the point spread function (Chandra Proposers’ Guide 2002). The background was obtained from an annulus surrounding the source. The net count rate was  $\sim 0.149 \pm 0.003$  counts  $\text{s}^{-1}$ .

A response matrix was constructed specific to the off-axis angle of SN1978K. The matrix was corrected for the time-dependent absorption using the fitted functional form which depends upon a single parameter, the time from launch; for this observation, the time from launch was 1179 days (Plucinsky et al. 2003).

## 3. Analysis: *Chandra* ACIS

Given the sharp point spread function of the *Chandra* mirrors, we must be concerned with possible event pileup even though the large off-axis angle mitigates the effects of pileup considerably. The spectral analysis was undertaken using a pileup model (Davis 2001). The resulting fit indicated low or zero pileup. Given the broader point spread function of the *XMM-Newton* mirrors, there is no pileup of the EPIC-pn or MOS spectra from that instrument. The results of the fits to the *Chandra* and *XMM-Newton* spectra, to be described below, are very similar, as one expects for observations separated by  $\sim 2$  years of a slowly-evolving object. The similarity supports the conclusion of low or zero pileup. We further fit the spectra with both XSPEC (Arnaud 1996) and the Sherpa fitting engine (Freeman, Doe, Siemiginowska 2001) and obtained identical results.

We first used the best-fit models derived from the *ROSAT* PSPC and *ASCA* SIS/GIS observations of SN1978K which consisted of absorbed, single-component continuum models (R93, Petre et al. 1994, S99). We fixed the model parameters at the previously-determined values, but it was immediately evident that the models no longer provided a good fit, instead yielding a  $\chi^2/\nu \geq 3$ . We then allowed the model parameters to vary; the resulting model fits remained poor. Figure 1 shows the fit using a single absorbed Raymond-Smith model. Clearly a single-component model is inadequate as it can not simultaneously fit the emission in the 0.7-1.2 keV region as well as the apparent hard component at energies above  $\sim 2$ -3 keV. That the *ROSAT* PSPC models do not provide a good fit is not especially surprising given the softer response of that detector. That the *ASCA* spectra do not provide a good fit may be explained as either an increase in flux above 2

keV by a factor of  $\sim 4$  since 1995 or by the difficulty in carrying out background subtraction for the *ASCA* spectra stemming from the large ( $\sim 1'.5$ ) point spread function. Indeed, the fit to the *ASCA* spectra suggests the presence of a harder component that was not statistically significant. We believe a factor of 4 is too large to be ascribed to difficulties with background subtraction.

We then explored a variety of models. We do not include a long discussion of those models that failed, but instead focus on the more successful ones. Most of the models failed by missing flux in the 0.8-1.0 keV band, a region known to contain the potential for considerable line emission. Table 1 includes a listing of the models ranked by increasing  $\chi^2/\nu$ . The ‘dual brems’ and ‘brems+multi-gauss’ models yield adequate fits but leave systematic residuals. The non-equilibrium ionization model (in ‘xspec’ lingo, ‘nei’; Borkowski, Lyerly, & Reynolds 2001 and references therein), the plane-parallel shock model (‘pshock’; Borkowski, Lyerly, & Reynolds 2001) as well as other shock models also provided adequate fits, but did not achieve the lowest  $\chi^2$  values. The ionization equilibrium collisional plasma model (‘equilib’) yielded a very poor fit. The single component power law, bremsstrahlung, and Raymond-Smith models were included for direct comparison with the historical results from *ROSAT* and *ASCA* (e.g., S99, Petre et al. 1994).

The best-fit model was an absorbed, two-temperature, optically thin thermal plasma model (the variable Mekal model ‘vmekal’ in xspec lingo that uses the line calculations of Mewe, Gronenschild, & van den Oord (1985), Mewe, Lemen, & van den Oord (1986), and Kaastra (1992) plus the Fe L enhancements of Liedahl, Osterheld, & Goldstein (1995)). Figure 2 shows the fitted spectrum. The best-fit temperatures are  $0.61_{-0.05}^{+0.04}$  and  $3.16_{-0.42}^{+0.44}$  keV and are shown as the *upper* set of contour plots in Figure 3 (the lower set of contours in each figure will be discussed shortly). The model-derived fluxes are listed in Table 2 and generally fall in the range of  $4\text{--}7 \times 10^{-13}$  erg s $^{-1}$  cm $^{-2}$  in the 0.5-2 keV band and  $\sim 3\text{--}4 \times 10^{-13}$  erg s $^{-1}$  cm $^{-2}$  in the 2-10 keV band with the low numbers corresponding to the absorbed flux and the high to the unabsorbed. These fluxes correspond to a 0.5-2 keV luminosity of  $\sim 7.5\text{--}14 \times 10^{38}$  erg s $^{-1}$  and a 2-10 keV luminosity of  $\sim 6\text{--}7.5 \times 10^{38}$  erg s $^{-1}$ .

The best-fit column,  $\sim 2.3 \times 10^{21}$  cm $^{-2}$  and shown in Figure 3, lies about a factor of 8–10 above the measured column in the direction of NGC 1313,  $\sim 3.7 \times 10^{20}$  cm $^{-2}$  (Schlegel, Finkbeiner, & Davis 1998). However, it does correspond to within 30% with the  $E_{B-V}$  value of 0.31 measured from optical spectra (Ryder et al. 1993) and using the  $N_{\text{H}}\text{--}E_{B-V}$  conversion of Predehl & Schmitt (1995):  $N_{\text{H}} \sim 5.3 \times 10^{21} E_{B-V}$ .

The vmekal model permits varying the abundances of astrophysically-important elements. We varied the abundances of each element in turn but forced the corresponding abundances of the soft and hard components to vary simultaneously but independently. This approach ensured the most robust detection of specific line features as well as differences between the soft and hard components. The only abundance inconsistent with solar is that of Si for the soft component. Figure 4 shows the uncertainty contours for the abundance of Si. The soft component abundance is 3.20 which is significantly different from solar at the 90% confidence level. The Si abundance for the hard component is consistent with solar. The fluxes for each component are listed separately in Table 2.

#### 4. Analysis: *XMM-Newton*, *ASCA*, & *ROSAT*

We also extracted spectra from the *XMM-Newton* observation of 2000 October 17. The observation lasted for 42416 sec but high background significantly constrained the extracted spectra to shorter times. The EPIC pn spectrum totaled 15940 s with an average rate of 0.263 counts s<sup>-1</sup>; the MOS-1 and MOS-2 spectra totaled 23838 and 24124 sec, respectively, at an average count rate of 0.088 and 0.089 counts s<sup>-1</sup>. Just under 50% of the total extracted counts formed the pn spectrum.

We fit the pn and MOS spectra using the best-fit *Chandra* model, namely the dual variable Mekal model. Table 3 lists the resulting model parameters. The fitted spectrum is shown in Figure 5. The best-fit temperatures are 0.67 and 2.87 keV. Rather than plot the parameter contours separately, we included them on the *Chandra* ACIS plots of Figure 3; the *XMM-Newton* contours are the *lower* set of contours in each figure. Note that the temperatures measured from the two instruments are essentially identical within the errors; the contours differ only in N<sub>H</sub> by a factor of ~1.65. One possible explanation is an increasing column density as the material cools and recombines.

The inferred luminosity in the soft band depends very sensitively on the adopted value for N<sub>H</sub>; because of that sensitivity, we adopt for N<sub>H</sub> a value determined from the measured E<sub>B-V</sub> for the *ROSAT* HRI and PSPC spectra as well as the *ASCA* spectra. This approach assigns a reasonable value to N<sub>H</sub> for the HRI data points for which no spectral information would otherwise be available. In addition, adoption of an E<sub>B-V</sub>-determined value for N<sub>H</sub> removes the artificially high value determined from fits to the *ASCA* spectra for which the calibration below ~0.7 keV is uncertain (Sambruna et al. 2000). We use the *Chandra*- and *XMM-Newton*-determined values of N<sub>H</sub> to probe the sensitivity of the unabsorbed fluxes to the adopted values.

For direct comparison of the *Chandra* and *Newton* results with the previously-described *ASCA* spectra (Petre et al. 1994, S99), we re-fit the *ASCA* spectra using the dual variable Mekal model as well as a single variable Mekal model. We included a single variable Mekal model to test whether the dual model is statistically required to fit the SIS spectra. Necessarily, the lower count rate yields larger error bars for each parameter of the dual Mekal model. We restrict our attention solely to the SIS spectra to ensure the best sensitivity to line emission. The fitted parameters values are listed in Table 3 while the fluxes are listed in Table 2. From the  $\chi^2/\nu$  values, the dual variable model provides a statistically better fit.

For the *ROSAT* PSPC and HRI fluxes, we re-extracted and re-fit the PSPC spectra using a single variable Mekal model. A dual model is not statistically required to provide a good fit largely because of the narrow bandpass. All of the abundance values were consistent with solar, within the errors, so we froze all at solar values. Unabsorbed fluxes were calculated in the 0.5-2 keV band. As HRI does not possess spectral resolution, we must adopt a fixed spectral model. We used a ‘best fit’ model of a single variable Mekal spectrum at kT = 0.6 keV and N<sub>H</sub> = 1.8×10<sup>21</sup> cm<sup>-2</sup>. This spectrum is essentially an average of the PSPC spectra and adopting the E<sub>B-V</sub>-determined N<sub>H</sub> value. Only the model normalization was adjusted for each HRI point. Unabsorbed fluxes in

the 0.5-2 keV band were then calculated. As a check, we converted count rates using the PIMMS<sup>1</sup> code; all of the converted values were within the errors of the calculated unabsorbed fluxes. We expect the fluxes are accurate within 25-30%.

## 5. Light Curves

From the collected set of unabsorbed fluxes, we constructed a light curve of the X-ray emission of SN1978K including an upper limit from the *Einstein* IPC reported in Ryder et al. (1993); Schlegel, Petre, & Colbert (1996) in the soft (0.5-2 keV) and hard (2-10 keV) bands.

The soft band light curve (Figure 6) shows immediately that the behavior in the 0.5-2 keV band is completely determined by the adopted value for the column density. Formally, we see a  $\sim 20\%$  decline from the *ASCA* epochs but within the errors, the light curve may still be interpreted as constant.

The hard band light curve (Figure 7) shows a decline of about a factor of 1.5 (mean *ASCA* values  $\sim 6.5 \times 10^{-13}$  erg s<sup>-1</sup> cm<sup>-2</sup> vs. *XMM/Chandra* values of  $\sim 4 \times 10^{-13}$  erg s<sup>-1</sup> cm<sup>-2</sup>). If the factor 1.5 decline is indicative of a future trend, then the peak occurred approximately 6000 days post-maximum, or near October 1994. For both the soft and hard light curves, the ‘peak’ is broad.

The *XMM-Newton* and *Chandra* points may be samples from a ‘hesitation’ on the decline. Such behavior, while completely speculative without additional observations, nevertheless is not without precedent - SN1979C (Montes et al. 2000) and SN2001ig (Ryder et al. 2003) both showed hesitations or outright increases during the decline phase of the radio light curves. The corresponding X-ray behavior is wholly unknown.

The behavior of the X-ray light curves is in contrast to the radio light curves all of which peaked considerably earlier. The fitted times of radio maximum differ because the radio light curve behavior is a function of frequency. However, the band with the latest peak, L at 1.38 GHz, reached a maximum near age 2000 days, or approximately November 1983 (S99), or about 11 years earlier.

## 6. Discussion

The apparent decline in the hard band vs. the soft band coupled with the potential emergence of a Si emission line signal the increasing transparency of the circumstellar medium surrounding SN1978K. If the X-ray transparency is increasing, then SN1978K has started its decline toward its remnant stage. Future observations will reveal the trend more concretely. We expect increasing line emission in the coming years.

---

<sup>1</sup>PIMMS=Portable, Interactive Multi-Mission Software; Mukai (1993).

However, we must be more cautious as the possibility exists that the column density is increasing as the material behind the shock recombines. A conclusion that the column density is increasing is at this point premature, resting as it would on two data points (the *Chandra* and *XMM* spectra). The *ASCA* spectra insufficiently constrained the column density to provide measurements of the trend over a longer time base. A future observation with *Chandra* or *Newton* would, with similar statistics per spectral channel, establish the nature of any trend that may exist.

The power law indices ( $n, s$ ) of the density profile of the ejecta ( $\rho_{\text{ejecta}} \propto r^{-n}$ ) and circumstellar matter distribution ( $\rho_{\text{cs}} \propto r^{-s}$ ) are important parameters of interaction models. They may be calculated from the light curve and from the ratio of the temperatures of the forward and reverse shocks (e.g., Fransson et al. 1996).

We interpret the temperatures of the two components as the temperatures of the forward and reverse shock emission. Fransson et al. (1996) show that the temperature ratio depends upon the circumstellar and supernova ejecta density distributions as  $T_r/T_f = (3 - s)^2/(n - 3)^2$ , where  $s$  = circumstellar density distribution exponent, usually 2 for a constant and homogeneous stellar wind, and  $n$  = SN ejecta density distribution exponent. The ratio of the temperatures of the two model fits to the *Chandra* spectrum is  $0.61/3.2 = 0.19$ ; solving for  $n$  yields an index of  $5.25 \pm 0.25$ . Repeating the same arithmetic for the *XMM-Newton* spectrum yields an index of  $5.07 \pm 0.10$ . An index of  $\sim 5$  is lower than usually adopted for the ejecta distribution; for example, Chevalier & Fransson (1994) derive results covering the index range of 7-12.

We argue, however, that  $n \sim 5$  is reasonable. Recently, Zimmermann & Aschenbach (2003) described an *XMM-Newton* observation of SN1993J in M81 and obtained a best-fit spectrum using the dual variable Mekal model. They inferred  $n = 8.9$  from the fitted temperatures after fitting the light curve to obtain  $s \sim 1.65$ .

However, Fransson & Björnsson (1998) showed that for SN1993J the circumstellar matter density was not  $s \sim 1.65$  as they first estimated from the radio light curve (Fransson et al. 1996), but was  $s = 2$  because their initial analysis failed to include synchrotron self-absorption. Their correction implies that circumstellar matter distributions really are deposited with  $s = 2$ . We therefore recalculate the index value for SN1993J.

From their best-fit model, Zimmermann & Aschenbach (2003) obtained temperatures of  $0.34 \pm 0.04$  and  $6.54 \pm 4$  keV for the *XMM-Newton* spectrum. Adopting  $s = 2$ , we obtain a value of  $n$  of  $\sim 7.4_{-1.8}^{+1.5}$ , where the large error range, driven by the large error on the high-temperature component, just overlaps the  $s \sim 1.65$  value. The ejecta distribution index of SN1993J is slightly larger than the value for SN1978K, but the error range reaches nearly to the SN1978K value of  $n = 5$ .

Having established that an index of  $\sim 5$  is not substantially different from the the index of SN1993J, we briefly examine whether the difference is in fact sensible. From Chevalier & Fransson (1994), lower values for the index lead to smaller density contrasts between the forward and reverse shocks, and adiabatic shocks at early times. SN1978K was essentially constant for at least 3 years near the peak (from  $\sim$ day 5500 to day  $\sim$ 6500; S99) while SN1993J declined essentially from the

time of the explosion Swartz et al. (2003). The increase in flux of SN1978K from the *Einstein* upper limit suggests that absorption was critical at very early times. This behavior is consistent with the adopted model for Type II<sub>n</sub> supernovae, namely, an object with a dense circumstellar medium resulting from a dense wind. Furthermore, Fransson et al. (1996) showed that the cooling time increases for smaller values of  $n$ . The different behavior of SN1993J (fading from start) and SN1978K (rises, then constant) fit within the context of the circumstellar model. The surprise is the apparent extreme sensitivity across a small difference in  $n$ .

We caution the reader to consider these numbers skeptically. As pointed out by, for example, Swartz et al. (2003), extrapolation of the self-similar interaction model to phases beyond a few months to years is “inappropriate” to adopt their description. In particular, the forward shock rapidly moves into prior phases of mass loss from the progenitor which need not be distributed in a smooth  $r^{-2}$  profile as usually assumed. Numerical calculations become necessary, including radiative losses, particularly for the reverse shock. We note the presentation of Nymark & Fransson (2003) demonstrating that multiple temperatures exist in the shocked gas in contrast to the considerably simpler models adopted for the present analysis.

## 7. Conclusions

We conclude that the *Chandra* and *XMM-Newton* observations detected the first hints of increasing transparency of the matter surrounding SN1978K. The increasing transparency signals the start of its decline in the X-ray band.

The low-temperature spectral components remain essentially unchanged from the *ASCA* epochs except for the addition of the detected Si. Within the errors, the high-temperature components have also not changed; if we restrict our attention solely to the *XMM-Newton* and *Chandra* observations of 2000 and 2002, then we see a decline of a factor of  $\sim 1.5$ , consistent with an interpretation of increasing transparency. Additional X-ray observations will confirm or refute our interpretation.

If X-ray line emission is becoming increasingly visible, line emission in other bands may be expected to change depending upon the atomic cascades. An observation with the *HST* STI Spectrograph is clearly warranted; such an observation would also aid in sorting out the emission region and clarifying the nature of the line emission uncovered with the FOS observation (S99).

Additional X-ray observations over the coming years are important to investigate possible variations in the wind as well as detecting the expected developing line emission. If our interpretation is correct, then the decline phase commenced just within the past few years and provides an opportunity to observe the decline. Comparison with SN1987A will reveal differences likely attributable to the differing densities of the circumstellar media.

At least two radio-emitting supernovae have shown hesitations and increases on the decline, interpreted as enhanced mass loss during the late stages of stellar evolution prior to the progeni-

tor’s explosion (e.g., SN2001ig, Ryder et al. (2003); SN1993J, Zimmermann & Aschenbach (2003); SN1979C, Montes et al. (2000) and references therein). With the shock moving at about  $10^3$  times the wind velocity, continued X-ray and radio observations are expected to provide in a human lifetime an extended view of several thousand years of late wind and mass loss behavior of a massive star.

The research of EMS was supported by contract number NAS8-39073 to SAO. PK acknowledges partial support from NASA grant NAG5-7405 and *Chandra* grant GO2-3102X.

## REFERENCES

- Chandra Proposers’ Guide, Rev 5.0 (Cambridge, MA: Chandra X-ray Center)
- Astronomical Data Analysis Software and Systems V, A.S.P. Conference Series, Vol. 101, 1996, George H. Jacoby & Jeannette Barnes, eds., p. 17.
- Borkowski, K., Lyerly, W. J., & Reynolds, S. P. 2001, ApJ, 548, 820
- Chevalier, R. & Fransson, C. 1994, ApJ, 420, 268
- Davis, J. E. 2001, ApJ, 562, 575
- Dopita, M. & Ryder, S. 1990, IAU Circular 4950
- Fabbiano, G. & Trinchieri, G. 1987, ApJ, 315, 46
- Fabbiano, G., Trinchieri, G., & MacDonald, A. 1984, ApJ, 284, 65
- Fransson, C. & Björnsson, C.-I. 1998, ApJ, 509, 861
- Fransson, C., Lundqvist, P., & Chevalier, R. 1996, ApJ, 461, 993
- Freeman, P., Doe, S., & Siemiginowska, A. 2001, SPIE, 4477, 76
- Garmire, G. P., Bautz, Mark W., Ford, Peter G., Nousek, John A., & Ricker, George R., Jr., SPIE, 4851, 28
- Immler, S. & Lewin, W. 2002, astro-ph/020223
- Kaastra, J.S. 1992, An X-Ray Spectral Code for Optically Thin Plasmas (Internal SRON-Leiden Report, updated version 2.0)
- Liedahl, D. A., Osterheld, A. L., & Goldstein, W. H. 1995, ApJ, 438, L115
- Méndez, B., Davis, M., Moustakas, J., Newman, J., Madore, B. F., & Freedman, W. L. 2002, AJ, 124, 213

- Mewe, R., Gronenschild, E.H.B.M., and van den Oord, G.H.J. 1985, *A&AS*, 62, 197
- Mewe, R., Lemen, J.R., and van den Oord, G.H.J. 1986, *A&AS*, 65, 511
- Montes, M. J., Weiler, K. W., Van Dyk, S. D.; Panagia, N., Lacey, C. K., Sramek, R. A.; Park, R. 2000, *ApJ*, 532, 1124
- Mukai, K. 1993, *Legacy*, 3, 21 (available at <http://heasarc.gsfc.nasa.gov/docs/journal/journals.html>)
- Nymark, T. K. & Fransson, C. (2003), in *From Twilight to Highlight: The Physics of Supernovae*, eds. W. Hillebrandt & B. Leibundgut (Berlin: Springer), 315
- Petre, R., Okada, K., Mihara, T., Makishima, K., & Colbert, E. J. M. 1994 *PASJ*, 46, L115
- Plucinsky, P. P. et al. 2003, *X-Ray and Gamma-Ray Telescopes and Instruments for Astronomy*, ed. J. E. Trümper & H. D. Tananbaum, *SPIE*, vol 4851, pp89 (13 co-authors)
- Predehl, P. & Schmitt, J. H. M. M. 1995, *A&A*, 293, 889
- Ryder, S., et al. 2003, in preparation
- Ryder, S., Staveley-Smith, L., Dopita, M., Petre, R., Colbert, E. J. M., Malin, D., & Schlegel, E. M. 1993, *ApJ*, 416, 167 (R93)
- Sambruna, R. M., Chou, L. L., & Urry, C. M. 2000, *ApJ*, 533, 650
- Schlegel, D. J., Finkbeiner, D., & Davis, M. 1998, *ApJ*, 500, 525
- Schlegel, E. M., Ryder, S., Staveley-Smith, L., Petre, R., Colbert, E. J. M., Dopita, M., & Campbell-Wilson, D., 1999, *AJ*, 118, 2689 (S99)
- Schlegel, Eric M., Petre, R., & Colbert, E. J. M. 1996, *ApJ*, 456, 187
- Schlegel, Eric M., *Rep. Prog. Phys.*, 58, 1375
- Swartz, D. A., Ghosh, K. K., McCollough, M. L., Pannuti, T. G., Tennant, A. F., & Wu, K. 2003, *ApJS*, 144, 213
- Weiler, K. W., van Dyk, S. D., Sramek, R. A., & Panagia, N. 1996, in *Radio emission from the stars and the sun*, ed. A. R. Taylor & J. M. Paredes (San Francisco: Astronomical Society of the Pacific), 141
- Zimmermann, H.-U. & Aschenbach, B. 2003, *A&A*, 406, 969 (astro-ph/0304322)

## 8. Figures

Table 1: Spectral Model Fits to ACIS Spectrum<sup>a</sup>

Model	$\chi^2/\nu$	DoF	$N_H$ ( $\times 10^{22}$ cm <sup>-2</sup> )	Param-1	Param-2	Norm-1	Norm-2
Dual VMekal	1.20	100	$0.23^{+0.04}_{-0.03}$	$T_1=0.61^{+0.04}_{-0.05}$	$T_2=3.16^{+0.44}_{-0.40}$	1.4e-4	4.9e-4
+ vary Si	...	...	...	$Si=3.20^{+1.80}_{-1.90}$	$Si=0.70^{+1.20}_{-0.70}$	...	...
Dual Brems	1.62	99	$0.47^{+0.30}_{-0.02}$	$T_1=0.27^{+0.01}_{-0.10}$	$T_2=3.42^{+1.90}_{-2.10}$	2.8e-4	6.6e-2
+ Gauss <sup>b</sup>	...	...	...	$E_{line}=0.877^{+0.03}_{-0.10}$	$EqW=73^{+79}_{-46}$	...	...
+ Gauss <sup>b</sup>	...	...	...	$E_{line}=1.80^{+0.07}_{-0.02}$	$EqW=78^{+24}_{-44}$	...	...
Brems +	1.67	98	$0.17^{+0.04}_{-0.03}$	$T=1.89^{+0.41}_{-0.23}$	...	3.8e-4	...
+ Gauss <sup>b,c</sup>	...	...	...	$E_{line}=0.654$	$EqW=79^{+78}_{-38}$	...	...
+ Gauss <sup>b,c</sup>	...	...	...	$E_{line}=0.826$	$EqW=165^{+55}_{-46}$	...	...
+ Gauss <sup>b,c</sup>	...	...	...	$E_{line}=0.915$	$EqW=101^{+30}_{-41}$	...	...
+ Gauss <sup>b,c</sup>	...	...	...	$E_{line}=1.02$	$EqW=122^{+29}_{-54}$	...	...
+ Gauss <sup>b,c</sup>	...	...	...	$E_{line}=1.86$	$EqW=60^{+29}_{-54}$	...	...
P-shock	1.87	104	$0.69^{+0.03}_{-0.03}$	$T=2.29^{+0.60}_{-0.43}$	$\log \tau=9.954^{+0.059}_{-0.051}$	9.1e-4	...
NEI	2.06	104	$0.72^{+0.03}_{-0.03}$	$T=2.42^{+0.58}_{-0.42}$	$\log \tau=9.714^{+0.038}_{-0.035}$	8.4e-4	...
Powerlaw	3.12	105	$0.33^{+0.05}_{-0.03}$	$\Gamma=3.12^{+0.24}_{-0.17}$	...	5.5e-4	...
Brems	3.57	105	$0.18^{+0.02}_{-0.04}$	$T=1.25^{+0.32}_{-0.12}$	...	6.2e-4	...
Equilib <sup>d</sup>	4.59	105	0.06	kT=2.74	...	5.9e-4	...
Raymond-Smith	6.86	105	$0.08^{+0.04}_{-0.03}$	$T=1.09^{+0.02}_{-0.02}$	...	3.3e-4	...

<sup>a</sup>All errors listed are 90%. Units are  $10^{22}$  cm<sup>-2</sup> for  $N_H$ , keV for kT; eV for line energy and line widths.

<sup>b</sup>Gaussian line width fixed at 0.0 to model an unresolved line; the line is broadened by the intrinsic energy resolution of the ACIS detector.

<sup>c</sup>Gaussian line energy fixed at listed value.

<sup>d</sup>No error bars are included on “Equilib” because the fit was too poor. Error bars would not normally be included for the others because of the poor fits but are so included for comparison with the historical *ROSAT* and *ASCA* results.

Table 2: Fluxes for Best-Fit Models: *Chandra*, *XMM-Newton*, and *ASCA*<sup>a</sup>

Satellite	Age <sup>b</sup> (days)	Band	Complete Model		Soft Component		Hard Component	
			Absorbed	Unabsorbed	Absorbed	Unabsorbed	Absorbed	Unabsorbed
Chandra	8910	0.5-2	3.80±0.57	7.26±1.09	1.66±0.25	3.59±0.54	2.13±0.32	3.66±0.55
		2-10	3.87±0.23	3.98±0.24	0.10±0.01	0.11±0.01	3.81±0.23	3.92±0.24
XMM	8184	0.5-2	4.61±0.41	6.86±0.62	1.87±0.17	2.98±0.27	2.72±0.24	3.88±0.35
		2-10	3.92±0.01	3.95±0.16	0.11±0.01	0.12±0.01	3.76±0.18	3.83±0.16
ASCA-1 <sup>c</sup>	5531	0.5-2	4.86±1.38	8.49±2.07	2.25±0.72	4.30±1.39	2.61±0.64	4.19±1.03
		2-10	5.91±1.67	6.05±1.47	0.14±0.04	0.15±0.05	5.77±1.41	5.90±1.45
ASCA-2 <sup>c</sup>	6401	0.5-2	5.38±3.16	13.7±8.07	3.13±1.84	6.31±3.72	3.11±1.83	4.98±2.93
		2-10	5.02±0.91	7.09±1.28	0.13±0.02	0.14±0.02	6.78±1.22	6.89±1.25

<sup>a</sup>All fluxes have units of  $10^{-13}$  erg s<sup>-1</sup> cm<sup>-2</sup>.

<sup>b</sup>Age in days past maximum, adopted to be 1978 May 22, MJD 43650.

<sup>c</sup>N<sub>H</sub> value of  $2 \times 10^{22}$  falls within fitted range and adopted for flux calculations.

Table 3: Model Fits to *XMM-Newton* and *ASCA* Spectra

Obs	Date	$\chi^2/\nu$	DoF	N <sub>H</sub> ( $10^{22}$ cm <sup>-2</sup> )	T <sub>soft</sub>	T <sub>hard</sub>	Norm-1 <sup>a</sup>	Norm-2 <sup>a</sup>
Dual VMekal model								
XMM	2000 Oct 17	1.19	308	0.15 <sup>+0.02</sup> <sub>-0.01</sub>	0.67 <sup>+0.03</sup> <sub>-0.03</sub>	2.87 <sup>+0.18</sup> <sub>-0.12</sub>	1.2e-4	5.2e-4
		...	...	...	Si=2.77 <sup>+1.30</sup> <sub>-1.27</sub>	Si=0.85 <sup>+0.65</sup> <sub>-0.65</sub>	...	...
ASCA-1 <sup>b</sup>	1993 Jul 12	0.76	37	<0.60	0.73 <sup>+0.27</sup> <sub>-0.33</sub>	4.42 <sup>+10</sup> <sub>-1.60</sub>	1.2e-4	6.6e-4
ASCA-2 <sup>b</sup>	1995 Nov 29	1.02	60	0.36 <sup>+0.40</sup> <sub>-0.17</sub>	0.60 <sup>+0.19</sup> <sub>-0.21</sub>	4.01 <sup>+7.0</sup> <sub>-1.20</sub>	2.9e-4	7.9e-4
Single VMekal model								
ASCA-1 <sup>b</sup>	1993 Jul 12	1.15	42	0.14 <sup>+0.20</sup> <sub>-0.12</sub>	1.06 <sup>+2.53</sup> <sub>-0.50</sub>	...	9.2e-4	...
ASCA-2 <sup>b</sup>	1995 Nov 29	1.20	64	0.67 <sup>+0.20</sup> <sub>-0.22</sub>	0.63 <sup>+0.07</sup> <sub>-0.08</sub>	...	1.7e-3	...

<sup>a</sup>Errors on normalizations are attached to the fluxes as listed in Table 2.

<sup>b</sup>Too few counts to fit Si abundance; value fixed at solar.

Table 4: Fluxes: *ROSAT* PSPC and HRI  
Approximate  
Observation

Detector	Date <sup>a</sup>	MJD	Age <sup>b</sup>	Flux <sup>c</sup> $\times 10^{-13}$
IPC	1980 Jan 2 <sup>d</sup>	44240	590	<1.2
PSPC	1990 Jul 11 <sup>e</sup>	48083	4433	13.7±3.8
PSPC	1990 Jul 23	48095	4445	8.3±3.4
PSPC	1991 Mar 18	48333	4683	4.7±3.0
PSPC	1991 Apr 24	48370	4720	7.8±1.6
HRI	1992 May 6 <sup>a</sup>	48748	5080	8.5±5.9
PSPC	1993 Nov 3	49294	5649	12.4±2.2
HRI	1994 Jul 9 <sup>a</sup>	49542	5888	11.3±3.2
HRI	1995 Feb 5 <sup>a</sup>	49753	6103	12.4±4.2
HRI	1995 Feb 6 <sup>a</sup>	49754	6104	10.5±2.8
HRI	1995 Apr 16 <sup>a</sup>	49823	6173	10.4±3.0
HRI	1995 Jun 15 <sup>a</sup>	49883	6233	11.5±2.7
HRI	1995 Jun 16 <sup>a</sup>	49884	6234	12.1±3.6
HRI	1997 Oct 4 <sup>a</sup>	50725	7076	9.1±2.8
HRI	1998 Apr 5 <sup>a</sup>	50908	7258	9.6±2.1

<sup>a</sup>MJD at center of observation when spanning multiple days; those observations are footnoted.

<sup>b</sup>units = days; based upon adopted date of maximum = 1978 May 22 = MJD 43650.

<sup>c</sup>All fluxes in 0.5-2.0 keV band with units of  $\text{erg s}^{-1} \text{cm}^{-2}$ . Adopted model is an absorbed vmekal,  $kT = 0.6 \text{ keV}$ ,  $N_{\text{H}} = 2.0 \times 10^{21} \text{ cm}^{-2}$ , based upon the the estimated value of  $E_{\text{B-V}}$  of 0.31 from Ryder et al. (1993).

<sup>d</sup>Observation obtained by *Einstein* IPC (Fabbiano, Trinchieri, & MacDonald 1984; Fabbiano & Trinchieri 1987).

<sup>e</sup>Observation obtained during *ROSAT* All-Sky Survey using PSPC-C. Sequence number = RS932904n00. See S99 for a listing of other sequence numbers.

Fig. 1.— Spectral fit to *Chandra* ACIS spectrum using a Raymond-Smith model adopted from the best-fit *ASCA* model (Petre et al. 1994). For this figure, only the model normalization was adjusted. Spectral evolution from the *ASCA* 1993 epoch is evident.

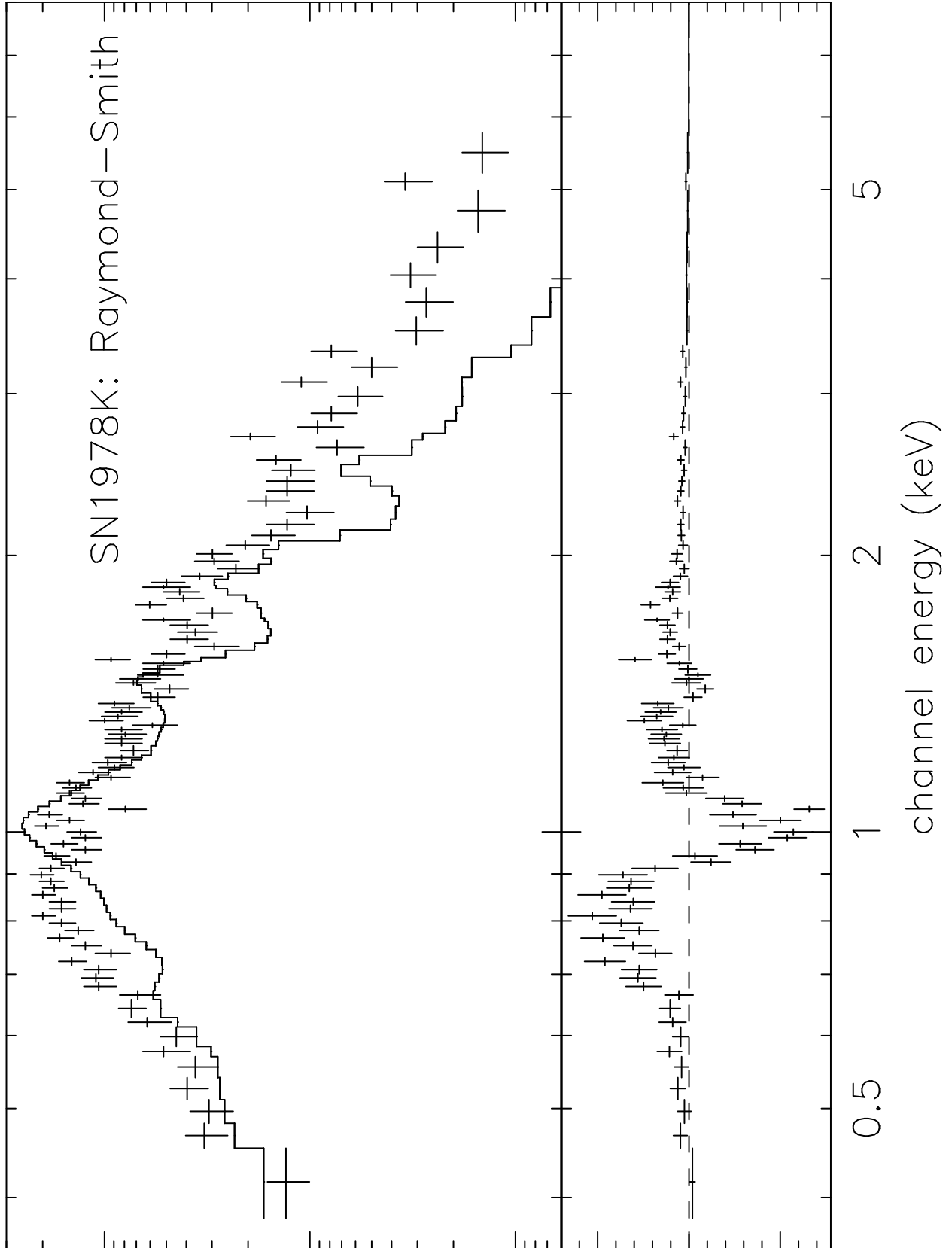


Fig. 2.— Dual variable Mekal model fit to the *Chandra* ACIS spectrum. The dashed lines show the individual model components. Note the strong Si emission in the model of the soft component.

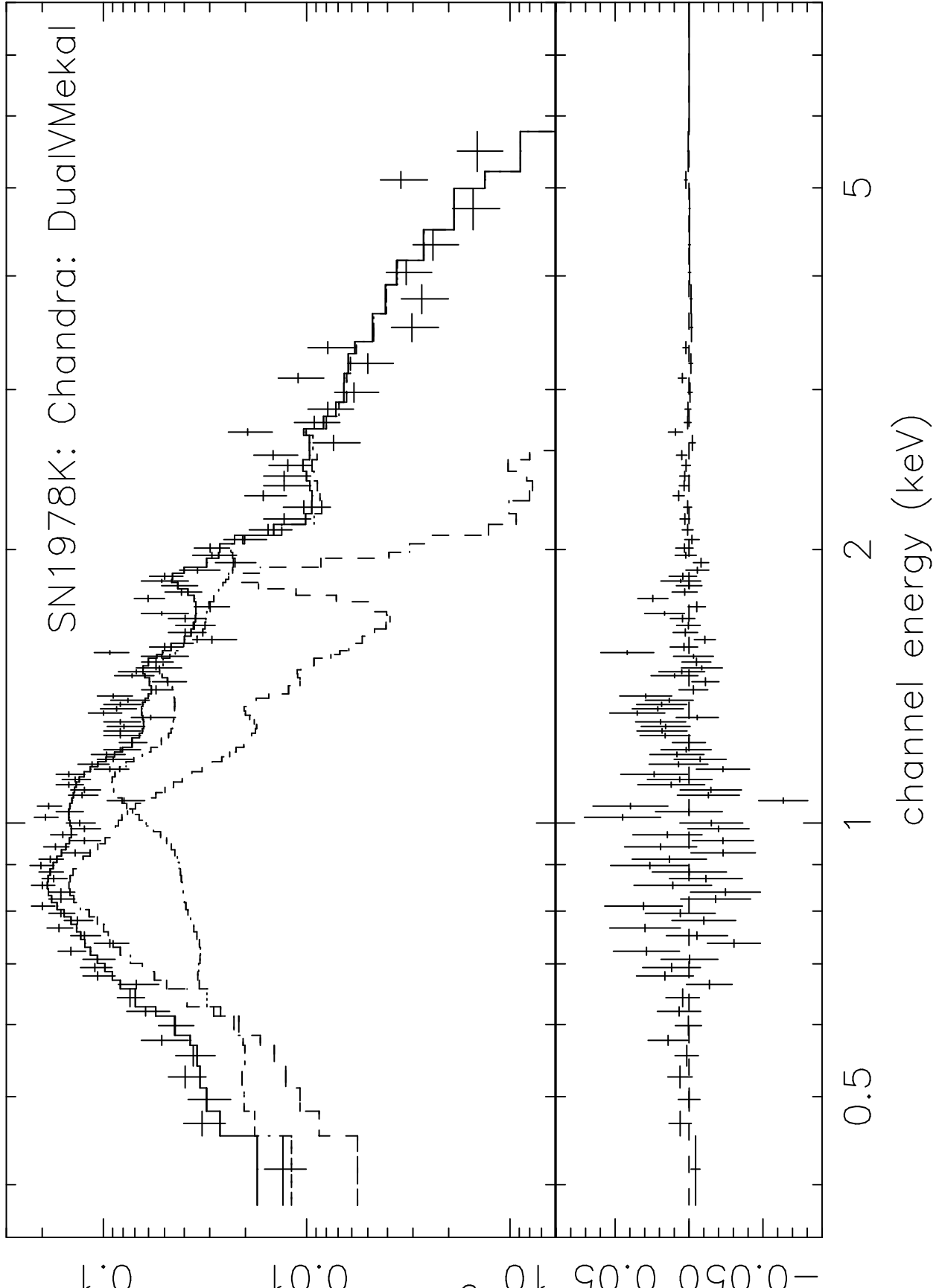


Fig. 3.— Contour plot for the (temperature, column density) parameters of the dual variable Mekal model for *Chandra* and *XMM-Newton*. The upper set of contours in each figure belong to *Chandra*, the lower set to *XMM-Newton*. a) low-temperature component and column density; (b) high-temperature component and column density.

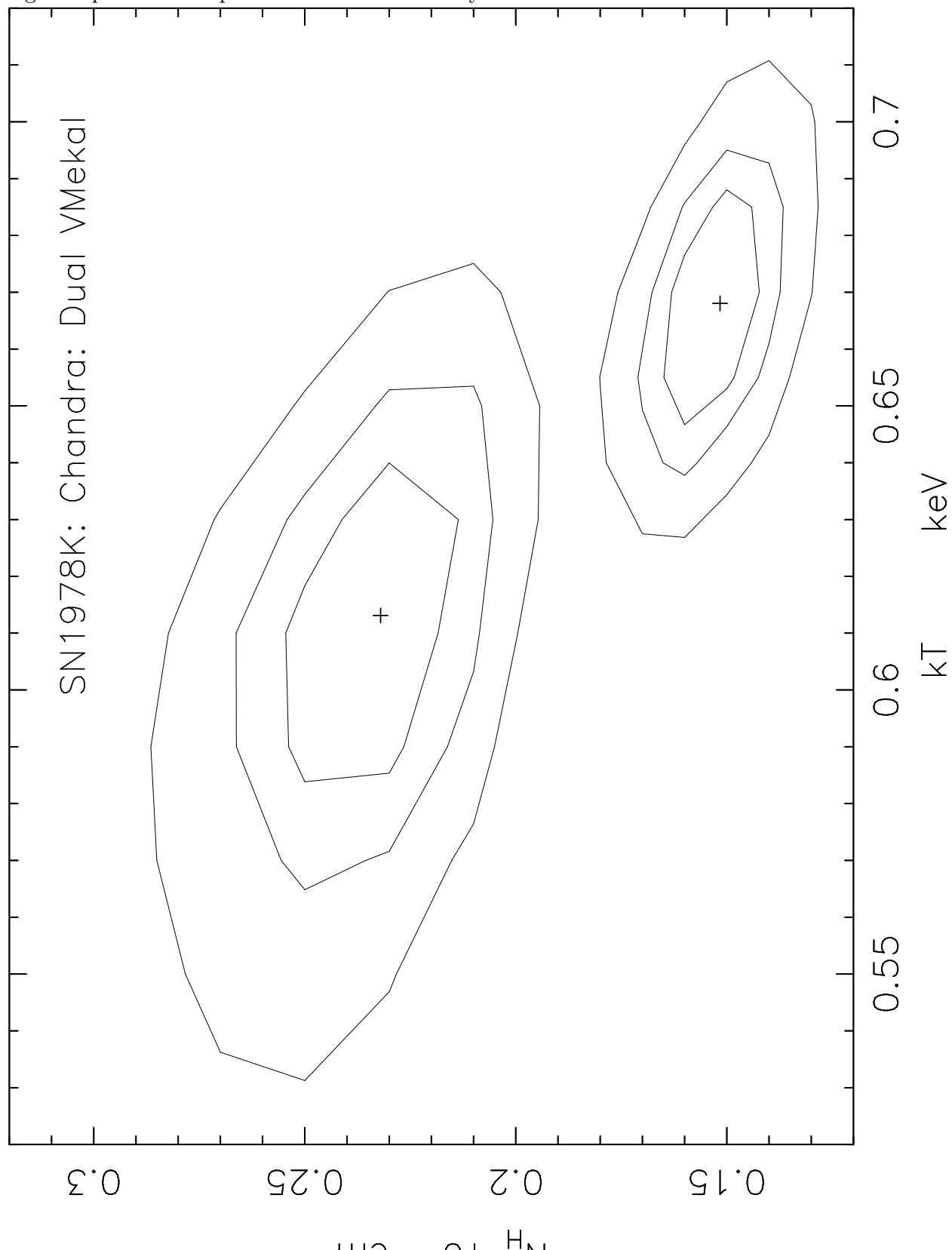


Fig. 4.— Contour plot for Si abundances for the dual variable Mekal model. Solid lines are the *Chandra* contours; dashed lines are the *XMM-Newton* contour. The Si abundances of the low-T components differ from solar at the 90% level (middle contour rings) while those of the high-T components are essentially undetermined.

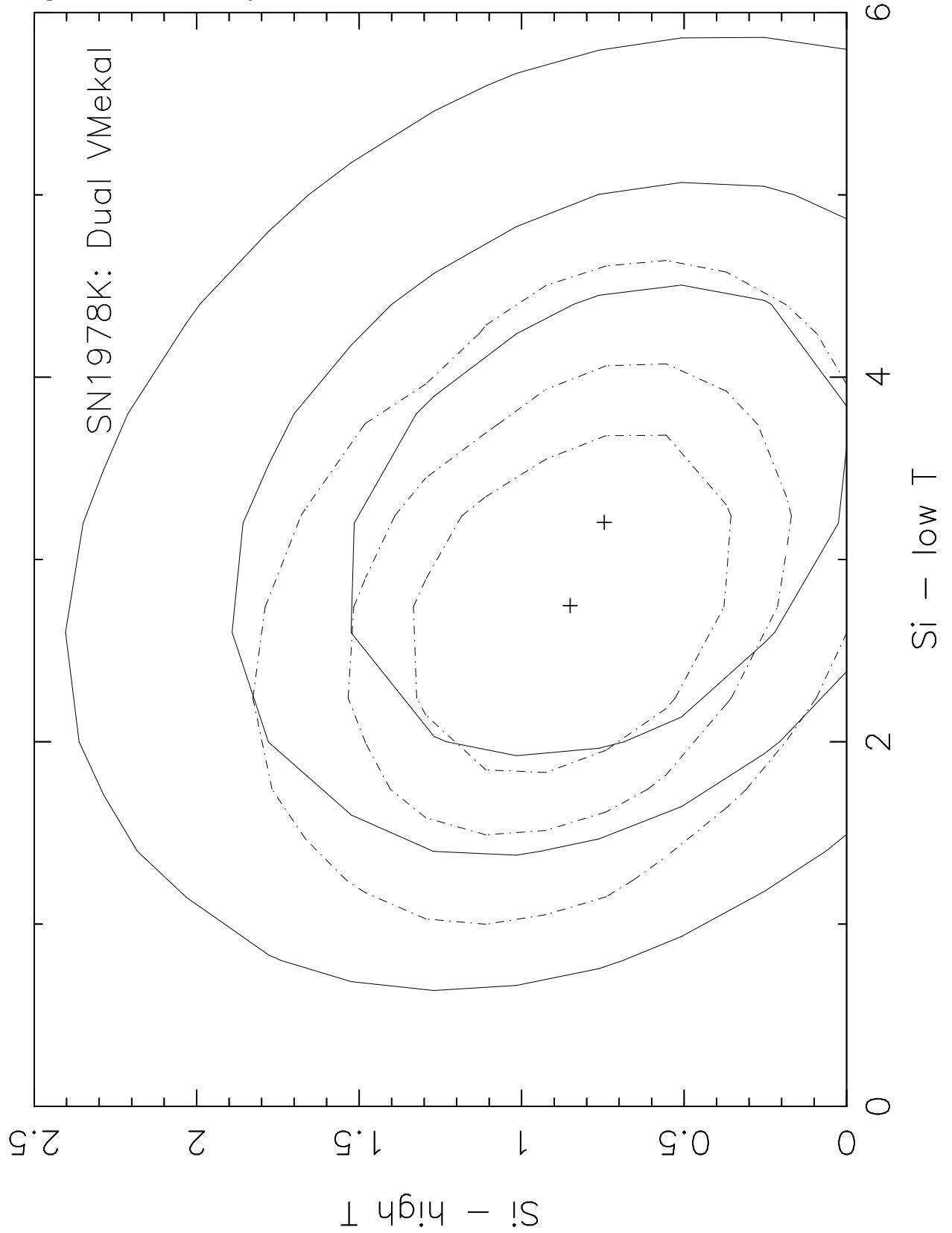


Fig. 5.— Plot of the *XMM-Newton* spectrum (EPIC pn, MOS-1, and -2) with the fitted dual variable Mekal model.

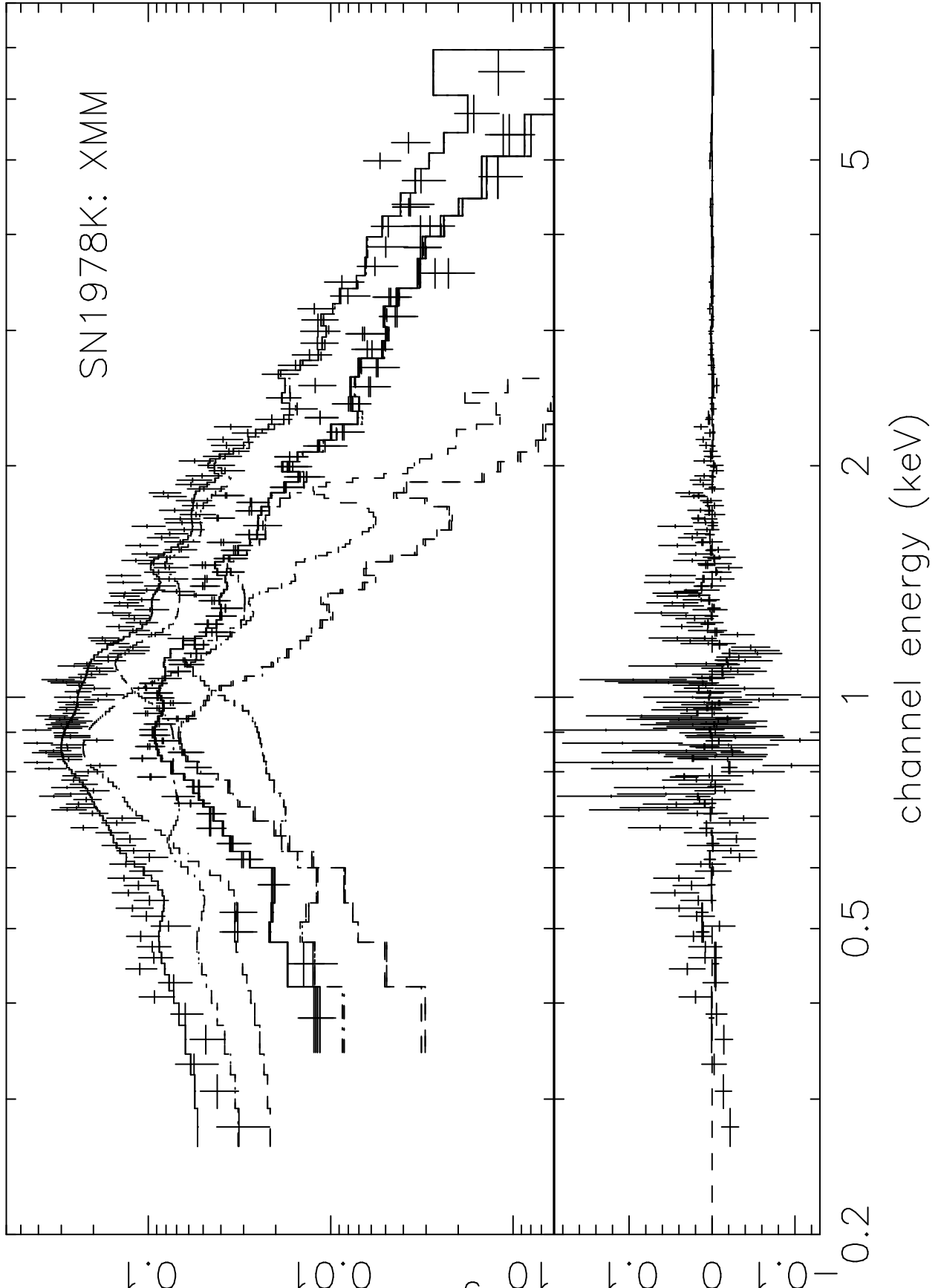


Fig. 6.— X-ray light curve in the 0.5-2 keV band based upon observations obtained with the *ROSAT* PSPC, *ROSAT* HRI, *ASCA* SIS/GIS, *XMM-Newton* EPIC, and *Chandra* ACIS and including an upper limit from an *Einstein* IPC observation (lower left corner).

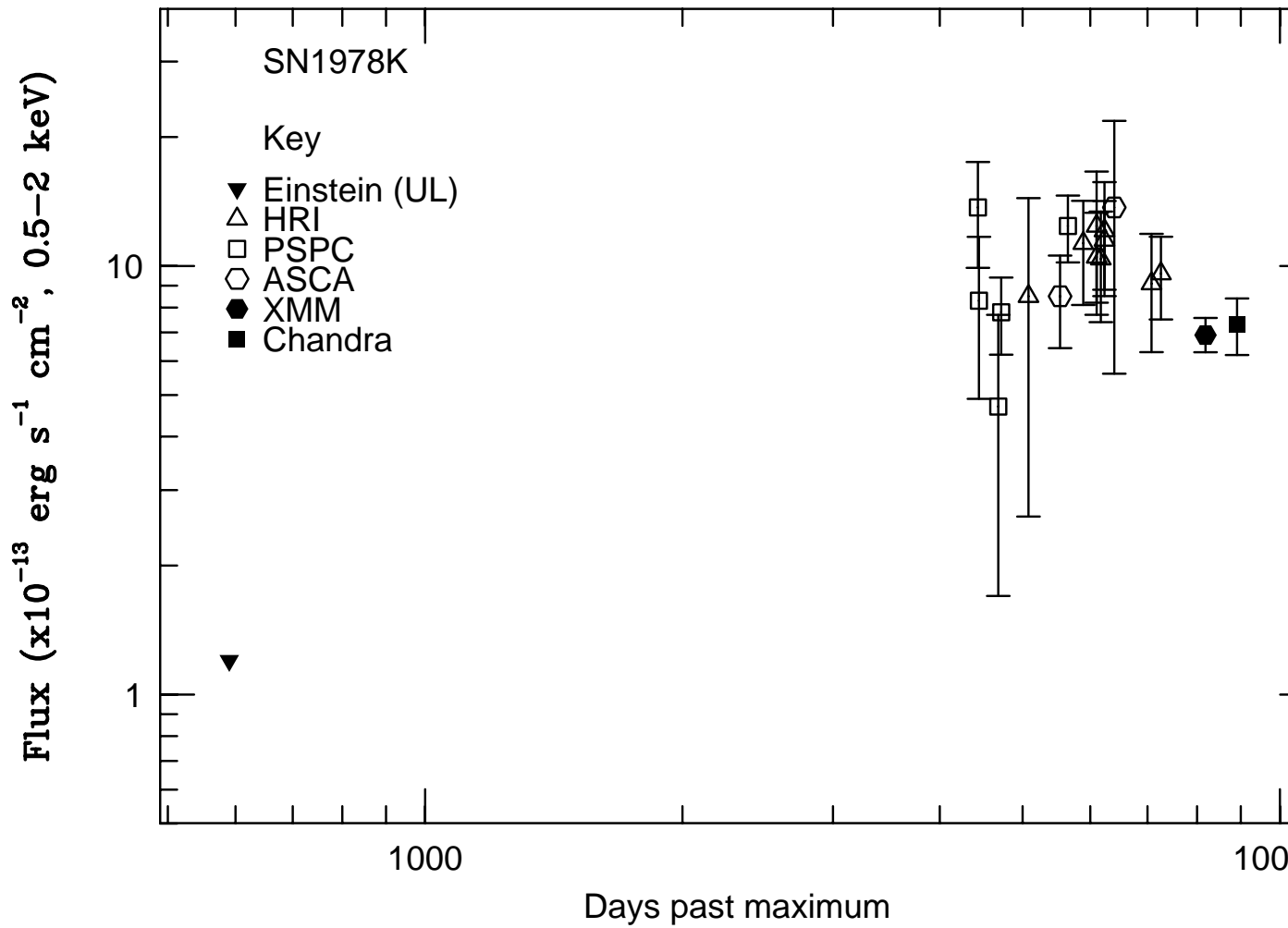


Fig. 7.— X-ray light curve in the 2-10 keV band based upon observations obtained with *ASCA* SIS/GIS, *XMM-Newton* EPIC, and *Chandra* ACIS and including an upper limit from an *Einstein* IPC observation (lower left corner). The IPC limit is extrapolated from the 2-4.5 keV band of the detector to the 2-10 keV band assuming a 3 keV bremsstrahlung model.

